# Chapter 8

# Pyrolysis of Peanut Shell: Optimization and Kinetics of Thermal Degradation Process

**Abstract**

The slow pyrolysis of peanut shell (PS) has been investigated using a TGA/DTG unit and a fixed-bed pyrolyser heating rates of 10, 15 and 20$^{o}$C/min and in the temperature range of ambient to 800$^{o}$C. The kinetic analysis of thermal degradation has been carried out using iso-conversional models. Effects of temperature, heating rate, and nitrogen gas flow rate on bio-oil and bio-char yields have been studied. The Box-Behenken design (BBD) of response surface methodology (RSM) has been used to optimize the process parameters. Bio-oil and bio-char have been characterized in terms of conventional thermo-chemical characteristics. The GC- Mass spectrometric, Fourier transform infra-red spectroscopic, and nuclear magnetic resonance spectroscopic analyses have been used to know the chemical constituents.

## 8.1 Introduction

Groundnut or peanut (*Arachis hypogaea* L.) is an important oil crop that is produced globally. It is an herbaceous plant that grows up to a height of 30 to 50 cm. The plant may be erect or prostrate and has a well-developed taproot having several lateral roots and nodules. The pods of peanut develop below ground and are 3 to 7 cm long and normally contain one to four seeds. Depending upon the variety and climatic conditions, peanut usually requires 100 to 150 days from planting to maturity. During 19$^{th}$ Century, West Africa became the primary source of peanut export (Pattee et al., 2005). It is now a major crop cultivated in tropical, sub-tropical, and warm temperate regions of Asia, Africa, Oceania, North and South America and Europe (Freeman et al., 1999). In 2014, peanut cultivation covered 25.7 million ha worldwide, including 13.1 million ha in Africa (51%), 11.2 million ha in Asia (44%) and 1.3 million ha in North and South America (5%) as per

FAO (2016). Climate, soil conditions and use of modern cultivation technology and crop management affect the yield per hectare. It has been reported that on an average it varies from 3 to 4 tons/ha, however, yields as high as 9.6 tons/ha too have been reported. The worldwide production of peanuts (with shells) was 40 million tons in 2015. Around 40% of this was produced in China, 19% in the other Asian countries, 18% in Africa and 11% in the Americas(USDA, 2016).India is the second largest (6.85million tonnes) producer of peanut after China (approximately 16.68 million tonnes per year) (FAO, 2016; Yao et al., 2016; Zhu et al., 2014) . Around 41% of the world peanut production is used for extracting oil and 45% is used as human food in the form of salted snacks, confectionary, peanut butter, nutritional bars, and several other dishes (FAOSTAT, 2014; Davis et al., 2016;Fletcher et al., 2016). Peanut with high aflatoxin content and peanut meal obtained after oil extraction are also used as animal feed (Myer et al., 2015; Hill et al., 2002).

On an average the peanut shell waste amounts to 350 to 400g per kg of pods produced. Thus the total global peanut shell waste biomass currently available globally will amount to around 16 million tons. The seed-skin, peanut stalk and spoiled peanuts are the other waste biomasses produced during peanut cultivation. In India and several other countries quite a sizeable amount of roasted peanut is sold by street vendors as cheap snack. The shell and skin produced through this type of use of peanut shell usually find their way to the domestic solid waste. As the peanut stalk has no use, it is left in the field or ploughed to be used as mulch. Very little attention is given to the utilization of peanut meal, shell, skin and stalk as an energy source. If these are also added to the peanut shell biomass waste, the total waste biomass will be much larger than that available from the peanut shell. It would be useful to assess the fuel potential of the waste biomass likely to be obtained through

peanut cultivation and processing of pods. In spite of the availability in large volume only a few workers have investigated the thermal degradation behavior of peanut shell biomass (Gurevich Messina et al., 2017; Yao et al., 2016; Zhu et al., 2014). In view of this in the present work an attempt has been made to evaluate the thermo-chemical characteristics and thermal degradation behavior of peanut shell biomass for assessing its potential as a renewable energy source.

### 8.2 Biomass collection and preparation

The waste peanut shell (PS) biomass was collected from the Lakhimpur Kheri (28.1651° N, 80.6327° E) district of Uttar Pradesh, India. It was washed with tap water to remove dirt particles and dried in air for 48h. The air dried sample was then placed in a hot air oven (Universal Oven, Model NSW-143(OUA-2) New Delhi, India) at $60^0$C temperature for 24h to prepare it for grinding. The oven dried sample was pulverized using a Wiley Mill (Model 2, Arthur H. Thomas Co. Philadelphia, USA). The powdered sample was sieved and particles of 177 μm average size were collected and kept in zipper poly-bags for use in further experiments.

### 8.3 Physicochemical characterization

The ASTM protocols (E-871, E-872 and D-1102, 2013) were used for evaluating ash, fixed carbon, moisture, and volatile matter contents. The estimation of C, H, N, and S was carried out using an elemental analyzer (Euro EA 3000, Elemental Analyzer Lombardi a Milano; Italy). The oxygen content was calculated by the difference. The higher heating value (MJ/kg) was estimated using a bomb calorimeter (RSB 3, Rajdhani Scientific Instruments Co. New Delhi, India) and the biological components (hemicellulose, cellulose

and lignin) were estimated by the van Soest's method (Bledzki et al., 2010; Soest et al., 1991).

### 8.4 TGA analysis and DTG analysis

The thermo-gravimetric analyses (TGA/DTG) was carried out using a TGA unit (Shimadzu, DTG-60, Kyoto, Japan, precision ±0.1 K) in nitrogen atmosphere from room temperature to 800$^{o}$C and at the heating rates of 10, 15 and 20$^{o}$C/min. In each case 10mg of sample was taken into the alumina crucible and the nitrogen gas flow rate was kept at 20 ml/min throughout the TGA experiments. The differential thermo-gravimetric analysis (DTG) data was generated using TGA data with the help of origin pro software.

### 8.5 Pyrolysis experiments

For slow pyrolysis experiments a lab-scale experimental setup shown in Fig.8.1was used. It consisted of a fixed-bed stainless steel tubular reactor (length: 520 mm; ID: 44 mm) mounted inside an electrically heated vertical tube furnace. Approximately 20g of accurately weighed sample was taken in each run. A constant flow of nitrogen gas (50mL/min) was maintained throughout the experiments to provide inert atmosphere and act as the carrier gas. The condensable vapors were collected in a bottle placed in an ice-bath. After attaining the set temperature, the heating was continued for additional 1h to collect all the condensable as liquid (bio-oil) and complete the char formation. The pyrolysis experiments were carried out in triplicate and average values (standard deviation of ± 1.0 %) are reported. The yields of pyrolysis product (aqueous bio-oil, gas and bio-char) were calculated using the formula:

$$Aq.Bio-oil\ Yield\ (wt\ \%) = \frac{Aq.Bio\ oil\ (g)}{Biomass\ feed\ (g)} X100 \quad (8.1)$$

$$Bio-char\ Yield\ (wt\ \%) = \frac{Bio-char\ (g)}{Biomass\ feed\ (g)} X100 \quad (8.2)$$

$$Gas\ Yield\ (wt\ \%) = 100 - \{Aq.Bio-oil\ Yield\ (wt\ \%) + Bio-char\ Yield\ (wt\ \%)\} \quad (8.3)$$

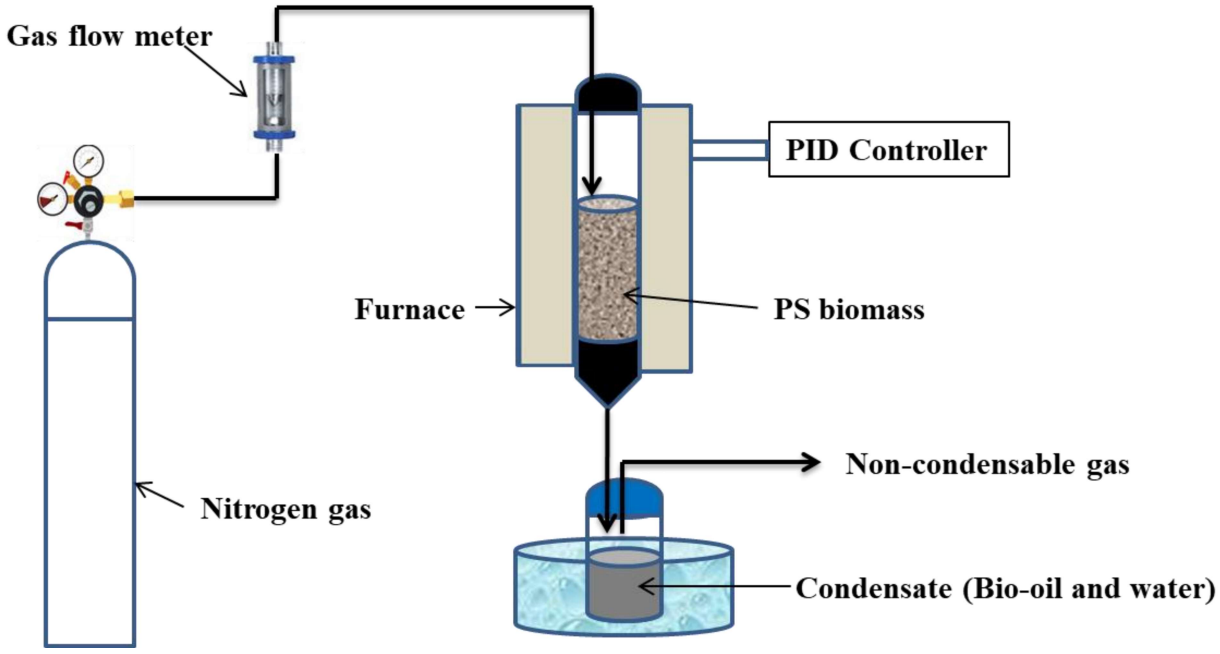


**Fig. 8.1** Block diagram of experimental setup

## 8.6 Experimental design

The design of process parameters for bio-oil and bio-char production using pyrolysis has been carried out using the response surface methodology (RSM, Version 10.0.6 Stat- Ease Inc. MNUSA). The Box-Behenken design (BBD) based on the Design Expert software (Stat-Ease's Design- Expert® Version 11 Software) was used to optimize the process

parameters- temperature (°C), heating rate (°C/min), and nitrogen flow rate (mL/min) for maximizing the yields of bio-oil and bio-char. These parameters were utilized at low (- 1), center (0), and high (+1) levels to investigate the quadratic model. Using the Box-Behenken design method, the number of experimental runs, was calculated from the number of factors, n to be optimized and number of repeated center points, using equation:

$$N = n^2 + n + r \qquad (8.4)$$

In total 17 experimental runs, comprising 12 unique runs and 5 center runs were performed to optimize the effect of process parameters on the response. The ranges of coded and experimental levels are presented in Table 8.1. The results were fitted in to the second order model given as:

$$Y = \beta_0 + \sum_{i=1}^{n} \beta_i X_i + \sum_{i=1}^{n} \beta_{ii} X_i^2 + \sum_{i=1}^{n} \sum_{j>1}^{n} \beta_{ij} X_i X_j \qquad (8.5)$$

**Table 8.1:** Experimental range of independent process variables

| Process variables | Level of experiments | | |
|---|---|---|---|
| | -1 | 0 | 1 |
| Temperature | 400 | 525 | 650 |
| Heating rate | 10 | 15 | 20 |
| Nitrogen flow rate | 50 | 100 | 150 |

### 8.7 ANOVA analysis

All the experimental runs were performed using the BBD design. Each experimental run was analysed using analysis of variance (ANOVA), coefficient of determination ($R^2$) and

contours and 3-dimensional diagrams were produced by the design expert software. It has been used for the data analysis of experimental design and the generation of the second order model. In the developed model the letters A, B, and C indicate the temperature, heating rate and nitrogen flow rate, respectively. It provides information regarding the statistical significance of various terms and assures the fitting of the model. Further, the model coefficients F and p values of ANOVA analysis signify whether the quadratic models are sufficient to explain the experimental data and also provide information about the significance or insignificance of the fitted model, respectively. The fitted model is statistically significant when the value of p is low ($p<0.05$) otherwise it is insignificant. Other parameter such as adequate precision which is the ratio of noise to signal is recommendable only when it is more than 4. For the optimization of processes the values of $R^2$, adjacent $R^2$ and predicted $R^2$ were considered.

**8.8 Pyrolysis product characterization**

The proximate and ultimate analyses of the bio-char were performed as per the ASTM standards as discussed for raw PS powder. The calorific values (MJ/kg) of the bio-oil and bio-char were evaluated using the digital bomb calorimeter mentioned earlier. The FTIR spectroscopic analyses were carried out using a FTIR spectroscope (5700 FTIR, Thermo-electron Cooperation Waltham, Massachusetts, United States) to know the functional groups of chemical compounds present in raw PS biomass and pyrolysis products. The NMR spectroscopic analysis of the bio-oil was carried out using a high resolution nuclear magnetic resonance spectrometer (Burker Bio Spin International AG, Model: AVH D 500 AVANCE III HD 500 MHz One Bay NMR Spectrometer, Billerica, Massachusetts, United States). The solvent for NMR analysis was deuterated dimethyl sulfoxide. The molecular

characterization of the bio-oil was carried out using a gas chromatography–mass spectrometry unit (Shimadzu-QP201, Kyoto Japan) equipped with Rxi-5 Sil MS column (30m×0.25mm×0.25μm film thickness)) to know the presence of various organic compounds.

**8.9 Kinetic and thermodynamic parameters**

The overall reaction for pyrolysis can be written as:

$$Biomass(solid) \xrightarrow{K(t)} Volatiles(condensable + noncondensable\ ) + Bio - char \qquad (8.6)$$

The non-isothermal iso-conversional methods were employed for evaluating the order of reaction, energy of activation and pre-exponential factor. For the iso-conversional pyrolysis process, the rate of change in conversion is given as (Poletto et al., 2012):

$$\frac{d\alpha}{dt} = K(T)f(\alpha) \qquad (8.7)$$

Whereα is defined as:

$$\alpha = \frac{m_0 - m_t}{m_0 - m_\infty} \qquad (8.8)$$

Theterm $(\frac{d\alpha}{dt})$ in Eq. (7) depends on the temperature dependent rate constant K(T) and reaction model f(α). The rate constant K (T) can be expressed by using the Arrhenius equation as:

$$K(T) = A\ exp\left(\frac{-\mathrm{E}}{RT}\right) \qquad (8.9)$$

Equations (8.7) and (8.9) on rearrangement give:

$$\frac{\mathrm{d}\alpha}{dt} = A\ exp\left(\frac{-E_\alpha}{RT}\right) f(\alpha) \qquad (8.10)$$

The term heating rate, β (°C/min) is introduced in Eq. 8.11 for the dynamic analysis of the non-isothermal data obtained using the TGA experiments as:

$$\beta = \frac{dT}{dt} = \frac{dT}{d\alpha}\frac{d\alpha}{dt} \qquad (8.11)$$

$$\frac{d\alpha}{dT} = \frac{A}{\beta} exp\left(\frac{-E_\alpha}{RT}\right) f(\alpha) \qquad (8.12)$$

Equation (8.12) can be integrated for the initial boundary condition, α = 0, at T = $T_0$to give:

$$g(\alpha) = \int_0^{\alpha} \frac{d\alpha}{f(\alpha)} = \int_0^{T} \frac{A}{\beta} exp\left(\frac{-E_\alpha}{RT}\right) dT \qquad (8.13)$$

For the constant heating rate data, Eq. 13 transforms to

$$g(\alpha) = \int_0^{T} \frac{A}{\beta} exp\left(\frac{-E_\alpha}{RT}\right) dT = \frac{AE}{\beta R} P(x) \qquad (8.14)$$

The term $P(x)$ has no analytical solution; therefore all iso-conversional methods adopt different mathematical approximations to solve the integral term. The assumptions and conditions utilized by Flynn-Wall and Ozawa (FWO)(Flynn, 1966), Kissinger-Akahira-Sunose (KAS) Akahira and Sunose, 1971), Tang (Wanjun et al. 2006), Starink (Starink,

2017), Vyazovkin (Vyazovkin, 1997), Vyazovkin AIC (Vyazovkin et al., 2011)to solve Eq. (8.14) and their relative advantages and disadvantages are given in Table 4.1.

## 8.10. Results and discussion

### 8.10.1. Physicochemical characteristics

The present results of proximate, ultimate and compositional analyses of PS together with the results of Agrawalla et al (2011), Collins et al (2018), Gurevich Messina et al (2017), Mohammed et al (2017), Yao et al (2016), Zhang et al (2002), and Zhu et al (2014) are presented as supplementary material(Table 8.2). The observed moisture content is low compared to the value reported by Collins et al (2018). The lower moisture content is desirable for thermal conversion of biomass. Energy used for removing the moisture content reduces the net available energy during pyrolysis and gasification (Kumar et al., 2019c). The observed volatile matter content 75.10% is in close agreement with the values reported for the peanut shell by other researchers (Gurevich Messina et al., 2017; Yao et al., 2016; Zhu et al., 2014). It has been reported that the higher amount of volatile matter results in higher yield of bio-oil (Cai et al., 2017). The conversion of most of the volatile matter content in to gaseous or liquid (aq. bio-oil) products, parameters like heating rate, temperature and reaction time are also important besides high content of the volatile matter (Cai et al., 2017). The observed fixed carbon content 18.43% is comparable to values reported by other researchers (Table 8.2). The ratio of volatile matter and fixed carbon, a measure of the availability of extractable energy content is 4.07% (Cai et al., 2017; Kumar et al. 2019a)**.** The observed ash content is lower compared to the previously reported values (Table 8.2). The high ash content is undesirable as it does not contribute to the energy

production and rather unfavourably affects the combustion and gasification processes (Motghare et al., 2016). The nature of the soil of the cultivated area and the water used for irrigation also affect the ash content. The values of carbon, hydrogen, nitrogen, oxygen and sulphur contents were found to be 58.71, 4.32, 2.72, 34.25 and 0% respectively (Table 8.2). The higher carbon content indicates high heating value of the sample. It is reported that the value of oxygen content is low compared to those reported by previous workers, which is advantageous for the bio-oil quality as the higher content of oxygen leads to the reduction in the heating value. The atomic ratios H/C and O/C are found to be 0.88 and 0.44, respectively. These ratios of any carbonaceous fuel indicate its combustion efficiency. The higher H/C ratio is more desirable than O/C (Kumar et al., 2019b).The cellulose content which is one of the major contributing fractions of any biomass for bio-oil production is found to be 53.45%. The hemicellulose and lignin contents were found to be 18.70 and 19.55%, respectively. The value of hemicellulose is comparable to the previously reported results while the lignin content is lower (Table 8.2).The higher heating value was found to be 18.95MJ/kg which is comparable to that of coal (Ashraf et al., 2019) and is higher than that of rice husk (Ashraf et al., 2019), sugar cane leaves (Kumar et al., 2019a), and banana trunk (Kumar et al., 2019c).

**Table 8.2:** Physicochemical properties of peanut/groundnut shell: Results of present and available published work

| Analyses | Present work | Collins et al (2018) | Agrawalla et al (2011) | Zhu et al (2014) | Yao et al., 2016 | Zhang et al (2001) | Gurevich Messina et al (2017) | Mohammed et al (2017) |
|---|---|---|---|---|---|---|---|---|
| **Proximate analysis (wt. %)** | | | | | | | | |
| Moisture content | 3.4 ± 0.31 | 8.00 | 5.60 | - | 1.16 | 7.40 | - | - |
| Volatile | 75.1 ± 0.39 | 64.63 | 83.00 | 76.50 | 71.36 | 66.20 | 73.60 | 65.40 |

| | | | | | | | | |
|---|---|---|---|---|---|---|---|---|
| Matter | | | | | | | | |
| Ash Content | 3.07 ± 26 | 5.91 | 4.80 | 13.90 | 6.81 | 10.40 | 5.90 | 5.70 |
| Fixed Carbon | 18.43 ± 0.32 | 29.45 | 6.60 | 9.60 | 20.67 | 16.00 | 20.50 | 19.60 |
| VM/FC | 4.07 ± 0.31 | - | - | - | - | - | - | - |
| Bulk density ($kg/m^3$) | 166 ± 1.5 | - | - | - | - | - | - | - |
| **Ultimate analysis (wt. %)** | | | | | | | | |
| C | 58.71 | 42.02 | 46.67 | 47.40 | 46.15 | 44.10 | 49.60 | 56.59 |
| H | 4.32 | 5.80 | 7.02 | 6.10 | 5.62 | 5.50 | 6.50 | 6.45 |
| N | 2.72 | 1.88 | 6.89 | 2.10 | 1.89 | 1.00 | 1.80 | 1.53 |
| O | 34.25 | 50.28 | 39.43 | 44.40 | 38.25 | 31.50 | 42.10 | 35.34 |
| S | - | - | 0.287 | - | 0.12 | 0.20 | - | 0.09 |
| H/C | 0.88 | - | 0.55 | - | - | - | - | - |
| O/C | 0.44 | - | - | - | - | - | - | - |
| **Compositional analysis (wt. %)** | | | | | | | | |
| Hemicellulose | 18.70 ± 0.23 | - | - | 18.70 | - | | 14.50 | - |
| Cellulose | 53.45 ± 0.26 | - | - | 35.70 | - | | 54.60 | - |
| Lignin | 19.55 ± 0.42 | - | - | 30.20 | - | | 30.90 | - |
| Extractives | 8.30 | - | - | - | - | | - | - |
| Calorific value (MJ/kg) | 18.95 | - | - | - | - | 17.70 | - | 16.40 |

### 8.10.2 FTIR spectra of peanut shell

The Fourier-transform infrared (FTIR) spectrum of raw PS depicted in Fig. 8.2 was obtained in the range of 400-4000$cm^{-1}$ to know the nature of the organic constituents

present through the identification of functional groups. The broad peak observed at 3400cm$^{-1}$ is attributed to hydroxyl (-O-H) functional groups of alcoholic, phenolic and water molecule (Collins et al., 2018). The low intense peak observed at 2900cm$^{-1}$ indicates the presence of C-H deformation group and is the strong evidence for the presence of alkanes. The peaks at 1600 and 1500cm$^{-1}$correspond to the O-H and C=O stretching and represent the existence of carboxylic acids and their derivative esters (Kumar et al. 2019b). The absorbance band near 1000cm$^{-1}$ is due to the C-O stretching and O-H deformation vibrations. This bond ascribes the presence of primary, secondary, and tertiary alcohols, ethers, and esters (Collins et al., 2018). The low intensity peak at 600cm$^{-1}$ indicates the existence of single, polycyclic, and substituted aromatic groups, as well as the C=O and C-O stretching indicate the existence of aromatic esters (Kumar et al., 2020a).

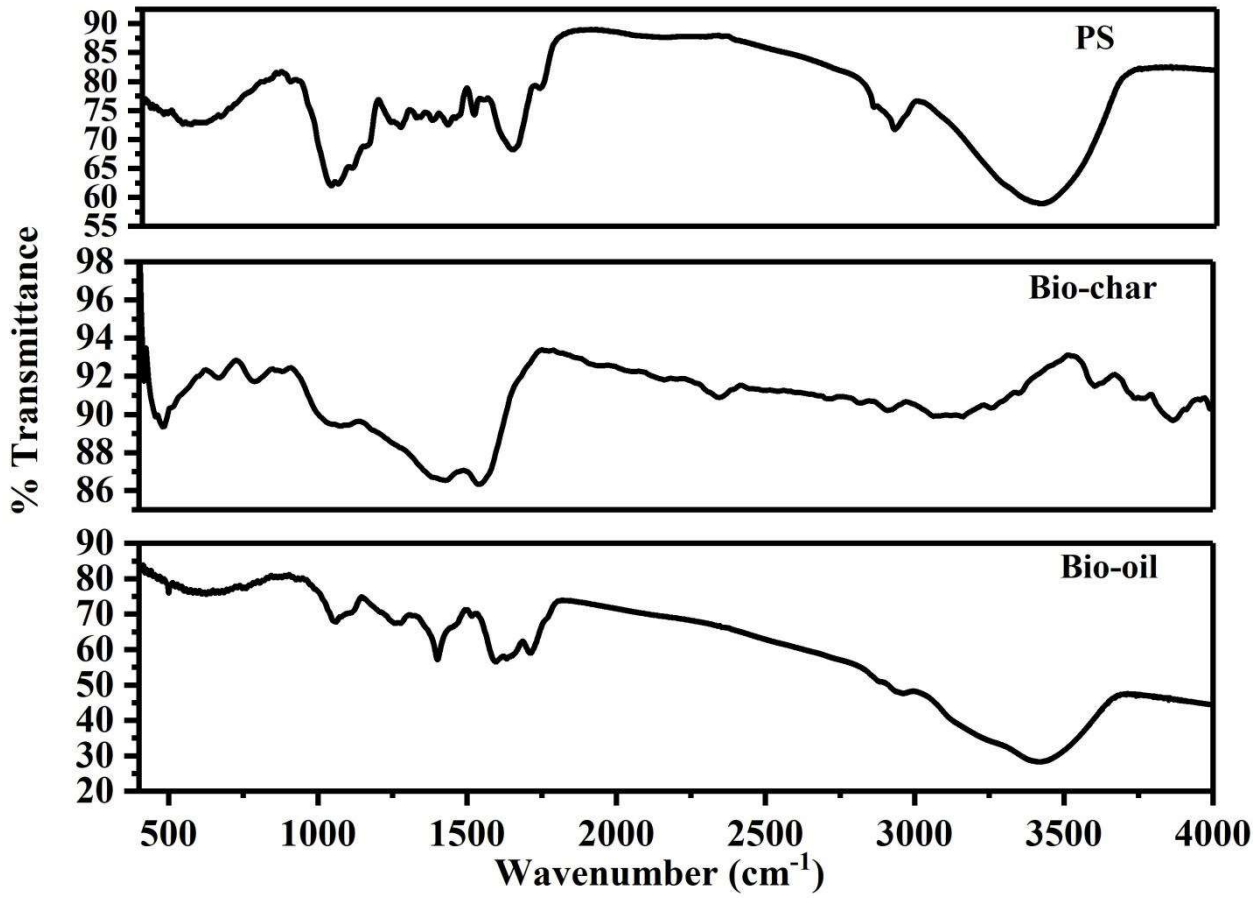


**Fig. 8.2** FTIR spectrum of raw, aq. bio-oil and bio-char

### 8.10.3 Thermal degradation analysis

The TGA and DTG versus temperature plots for heating rates of 10, 15 and 20°C/min are shown in (Fig. 8.3) and the data are given in Table 8.3.The TGA profile shows that the weight loss increases non-uniformly with temperature and its variation exhibits three different stages that can be attributed to the difference in the thermal stability of the constituents of PS. In Stage 1 (ambient to 220°C), mainly unbound and bound moisture and some light volatile compounds are removed from the biomass resulting in up to 10% weight loss. In Stage 2 (220 to 550°C), significant weight loss (up to 60%) occurs due to the degradation of hemicellulose, cellulose and some lignin. The hemicellulose

decomposes in the lower temperature range of 220 to 300$^{o}$Cdue to its poor thermal stability and lower degree of polymerization compared to cellulose and lignin. In the temperature range of 300 to 550$^{o}$C, the change in weight loss increases very sharply due to the degradation of the cellulose content. Finally in Stage 3 (550 to 800$^{o}$C), the residual lignin of the biomass is degraded slowly. In fact the thermal degradation of lignin occurs slowly throughout the temperature range of 200 to 800$^{o}$C. Due to its complex structure comprising of aromatic rings it is the most thermally stable component among all three constituents of a biomass and is responsible for the char formation in this stage.

The DTG-temperature profiles at different heating rate are depicted in Fig. 8.3. From these figures it is observed that the rate of percent degradation is very low (~ 1.5%/min) in Stage 1.In Stage 2 both weight loss and the rate of percent degradation increase with increasing temperature due to degradation of hemicellulose and cellulose molecules. The maximum rate of percent degradation is observed in the temperature range of 300-400$^{o}$C at all heating rates, this stage is commonly known as the ‘active stage’ of pyrolysis. In Stage 3 beyond 550$^{o}$C, the rate of percent degradation becomes sluggish and more or less constant at around 0.5%/min.

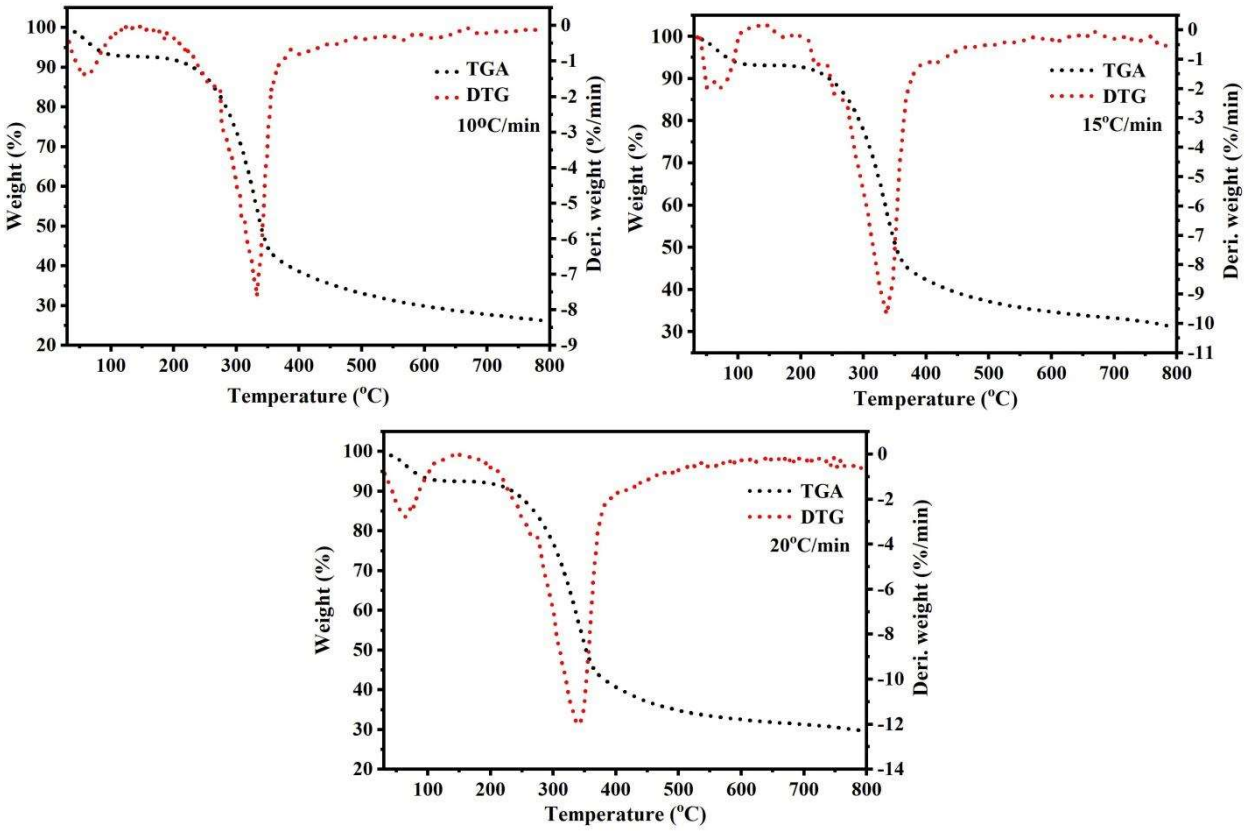


**Fig.8.3** Thermal degradation behavior of peanut shell at heating rates of 10, 15 and 20°C/min

### 8.10.4 Effect of heating rate on thermal degradation

Figure 3 shows the pyrolysis curves of PS at the heating rates of 10, 15 and 20°C/min and the relevant parameters are listed in Table 8.3. It is observed that the trend of weight loss remains the same at all heating rates due to nearly similar heat transfer mechanism to the individual particles. On increasing the heating rate from 10 to 20°C/min, the weight loss and the rate of percent degradation slightly decreased from 9.21 to 8.94%in Stage 1. In Stage 2, the rate of weight loss increased in the order of 7.94, 9.96 and 12.13%/min for the heating rates of 10, 15 and 20°C/min, respectively. The overall weight loss in this stage is more or less constant at all heating rates and is found to be approximately 60%. It is

observed that the TGA- and DTG-temperature curves and the temperature of the maximum weight loss are shifted slightly towards the higher temperature region. The amount of the residual char (bio-char) obtained in Stage 3 has increased from 26.29 to 31.25% with increase in heating rate from 10 to 20$^{o}$C/min.

**Table 8.3:** Thermal degradation: TG and DTG analysis

| Heating rate, β (°C/min) | Initial Temperature $T_i$ (°C) | Final Temperature $T_f$(°C) | Peak Temperature $T_P$ (°C) | -$DTG_{max}$ (%/°C) | Weight loss (%) | Residual weight (%) at 1000°C |
|---|---|---|---|---|---|---|
| **Stage I** | | | | | | |
| **10** | 28.07 | 220 | 61.29 | 1.40 | 9.21 | |
| **15** | 23.21 | 225 | 70.32 | 2.00 | 9.08 | |
| **20** | 21.77 | 230 | 64.73 | 2.79 | 8.94 | |
| **Stage II** | | | | | | |
| **10** | 235.04 | 550 | 332.80 | 7.94 | 59.34 | |
| **15** | 225 | 555 | 336.99 | 9.96 | 55.14 | |
| **20** | 230 | 560 | 337.66 | 12.13 | 57.37 | |
| **Stage III** | | | | | | |
| **10** | 550 | 800 | 556.00 | 0.40 | 5.16 | 26.29 |
| **15** | 555 | 800 | 610.42 | 0.41 | 4.63 | 31.15 |
| **20** | 560 | 800 | 761.52 | 0.58 | 3.69 | 31.25 |

### 8.10.5 Kinetic and thermodynamic parameters

The kinetic parameters were determined using iso-conversional kinetic models of KAS, FWO, Starink, Tang, Vyazovkin and Vyazovkin AIC approved by the Kinetics Committee of the International Confederation for Thermal Analysis and Calorimetry (ICTAC). Below 200$^{o}$C the evaporation of moisture and lighter organic molecules and their degradation occurs, between 200 to 600$^{o}$C most of the cellulose and hemicelluloses and some amount of lignin degrade and above 600$^{o}$C primarily lignin is degraded and char is formed, therefore the pyrolysis data in the temperature range of 200 to 600$^{o}$C were considered for the kinetic analysis at all heating rates. The values of conversion (α) were used from 0.1 to 0.9 as beyond this range the fitting of kinetic models was not good. The values of activation energy were evaluated from the slopes of the graphs plotted using the equations of the above mentioned models except for the Vyazovkin and Vyazovkin-AIC (V-AIC) models that require the use of an iteration technique and the activation energy was obtained at the minimum values of the corresponding functions shown in Table 4.1respectively. The values of activation energy at each conversion values are reported together with the corresponding average values for all six kinetic models are given in Table 8.4 and plotted in Fig. 8.4. It is seen that the activation energy versus conversion plots are exhibiting two general trends. The values obtained using KAS, Starink, and Tang models are almost the same and vary similarly with conversion, while the values for FWO, Vyazovkin, and Vyazovkin AIC models exhibit a different but nearly similar trend. In the conversion range of 0.1 to 0.8, the activation energy values lie between 165 to 225kJ/mol and for $\alpha > 0.8$ there is a steep rise. The difference in the activation energy obtained using these kinetic models can be attributed primarily to the difference in the mathematical expressions used

and their solution techniques. The KAS, Starink and Tang models use more or less similar mathematical assumptions and the FWO model uses a simple algebraic expression. The Vyazovkin model uses Senum-Yang approximation while Vyazovkin AIC requires the use of trapezoidal rule to solve the temperature integral in their respective expressions.

From Fig. 8.4 it is seen that the activation energy gradually increases in the conversion range of ($0.1 < \alpha < 0.3$) from 176 to 201.41kJ/mol for all the kinetic models. This behaviour can be attributed to the removal of the moisture and lighter organic molecules of increasing molecular weight from the biomass. In the conversion range of 0.4 to 0.8 the activation energy decreases from ~ 210 to 180kJ/mol for all the models and beyond this there is a steep rise in its value. This type of variation can be attributed to the change in the nature of the thermal degradation process due to difference in the rate of formation of degradation products and subsequent interactions between them. The observed steep rise for $\alpha > 0.8$ can be attributed to the degradation of lignin and formation of char.

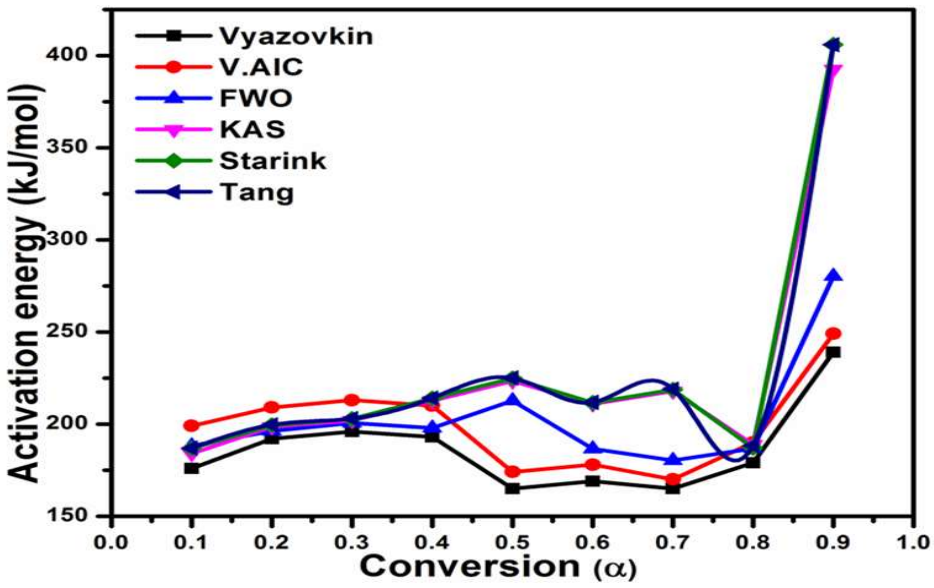


**Fig. 8.4** Variation of activation energy with conversion calculated using different models

**Table 8.4:** Values of activation energy, pre-exponential factor, and thermodynamic parameters with conversion levels calculated using iso-conversional models

| α | $E_\alpha$ (kJ/mol) | A* ($min^{-1}$) | ΔH* (kJ/mol) | ΔG* (kJ/mol) | ΔS* (J/mol.K) | $E_\alpha$ (kJ/mol) | A ($min^{-1}$) | ΔH* (kJ/mol) | ΔG* (kJ/mol) | ΔS* (J/mol.K) | $E_\alpha$ (kJ/mol) | A* ($min^{-1}$) | ΔH* (kJ/mol) | ΔG* (kJ/mol) | ΔS* (J/mol.K) |
|---|---|---|---|---|---|---|---|---|---|---|---|---|---|---|---|
| | | | FWO | | | | | KAS | | | | | Starink | | |
| **0.1** | 188.22 | 5.8E+13 | 183.75 | 180.00 | 6.02 | 183.96 | 2.5E+13 | 179.49 | 180.12 | -1.01 | 186.82 | 4.4E+13 | 182.35 | 180.04 | 3.71 |
| **0.2** | 196.28 | 2.9E+14 | 191.65 | 179.79 | 19.04 | 198.45 | 4.4E+14 | 193.80 | 179.73 | 22.61 | 199.36 | 5.3E+14 | 194.73 | 179.70 | 24.10 |
| **0.3** | 200.63 | 6.8E+14 | 195.87 | 179.67 | 25.99 | 201.96 | 8.9E+14 | 197.20 | 179.64 | 28.18 | 202.80 | 1.0E+15 | 198.04 | 179.62 | 29.57 |
| **0.4** | 197.88 | 3.9E+14 | 193.02 | 179.74 | 21.30 | 212.77 | 7.6E+15 | 207.90 | 179.37 | 45.80 | 213.93 | 9.5E+15 | 209.06 | 179.34 | 47.71 |
| **0.5** | 212.65 | 7.4E+15 | 207.67 | 179.37 | 45.40 | 223.33 | 6.1E+16 | 218.34 | 179.12 | 62.95 | 224.76 | 8.1E+16 | 219.77 | 179.08 | 65.30 |
| **0.6** | 186.63 | 4.3E+13 | 181.47 | 180.05 | 2.28 | 210.94 | 5.2E+15 | 205.78 | 179.41 | 42.32 | 211.55 | 5.9E+15 | 206.39 | 179.40 | 43.32 |
| **0.7** | 180.25 | 1.2E+13 | 174.98 | 180.23 | -8.42 | 217.89 | 2.0E+16 | 212.62 | 179.20 | 53.56 | 218.68 | 2.4E+16 | 213.41 | 179.23 | 54.86 |
| **0.8** | 186.70 | 4.3E+13 | 180.80 | 180.04 | 1.22 | 188.91 | 6.7E+13 | 183.01 | 179.98 | 4.86 | 187.10 | 4.7E+13 | 181.20 | 180.03 | 1.88 |
| **0.9** | 280.23 | 4.5E+21 | 274.07 | 177.94 | 14.10 | 392.54 | 1.6E+31 | 386.38 | 176.20 | 32.41 | 405.95 | 2.2E+32 | 399.79 | 176.02 | 33.80 |
| **Avg.** | 203.27 | 5.0E+20 | 198.14 | 179.65 | 14.10 | 226.97 | 1.8E+30 | 220.50 | 179.20 | 32.41 | 226.75 | 2.5E+31 | 222.75 | 179.16 | 33.80 |

| | | | Tang | | | | | Vyzovkin | | | | | V. AIC | | |
|---|---|---|---|---|---|---|---|---|---|---|---|---|---|---|---|
| **0.1** | 186.93 | 4.5E+13 | 182.46 | 180.04 | 3.88 | 176.00 | 5.1E+12 | 171.53 | 180.35 | -14.16 | 199.00 | 4.9E+14 | 194.53 | 179.71 | 23.78 |
| **0.2** | 199.58 | 5.5E+14 | 194.95 | 179.70 | 24.47 | 192.00 | 1.2E+14 | 187.37 | 179.90 | 11.98 | 209.00 | 3.6E+15 | 204.37 | 179.46 | 39.97 |
| **0.3** | 203.02 | 1.1E+15 | 198.26 | 179.61 | 29.92 | 196.00 | 2.7E+14 | 191.24 | 179.79 | 18.37 | 213.00 | 7.9E+15 | 208.24 | 179.36 | 46.34 |
| **0.4** | 214.15 | 9.9E+15 | 209.28 | 179.33 | 48.07 | 193.00 | 1.5E+14 | 188.13 | 179.87 | 13.26 | 210.00 | 4.3E+15 | 205.13 | 179.44 | 41.25 |
| **0.5** | 224.98 | 8.4E+16 | 219.99 | 179.08 | 65.66 | 165.00 | 5.8E+11 | 160.01 | 180.68 | -33.19 | 174.00 | 3.4E+12 | 169.01 | 180.41 | -18.30 |
| **0.6** | 211.79 | 6.2E+15 | 206.63 | 179.39 | 43.72 | 169.00 | 1.2E+12 | 163.84 | 180.56 | -26.83 | 178.00 | 7.7E+12 | 172.84 | 180.29 | -11.96 |
| **0.7** | 218.92 | 2.5E+16 | 213.65 | 179.22 | 55.25 | 165.00 | 5.8E+11 | 159.73 | 180.68 | -33.64 | 170.00 | 1.5E+12 | 164.73 | 180.53 | -25.36 |
| **0.8** | 188.27 | 5.9E+13 | 182.37 | 180.00 | 3.80 | 179.00 | 9.4E+12 | 173.10 | 180.26 | -11.49 | 190.00 | 8.3E+13 | 184.10 | 179.95 | 6.66 |
| **0.9** | 405.90 | 2.2E+32 | 399.74 | 176.02 | 34.35 | 239.00 | 1.3E+18 | 232.88 | 178.77 | -9.46 | 249.00 | 9.7E+18 | 242.84 | 178.55 | 12.79 |
| **Avg.** | 226.94 | 2.5E+31 | 223.04 | 179.16 | 34.37 | 186.00 | 1.5E+17 | 180.86 | 180.10 | -9.46 | 199.11 | 1.0E+18 | 193.98 | 179.75 | 12.79 |

Thermodynamic parameters ΔH, ΔG, and ΔS were calculated using pre-exponential factor (A) and activation energy (E) values using appropriate thermodynamic equations (Eq. 4.57 to 4.60).

The values of various parameters obtained using six kinetic models are given in Table 8.4 and variation with conversion are depicted in Fig 8.5. It is seen that the difference in the change in enthalpy and activation energy values obtained at each conversion level is nearly constant at ~5kJ/mol, which indicates the feasibility of the pyrolysis reaction. The small difference between E and ΔH also indicate that there is little requirement of external energy for the thermal conversion of biomass in to various products (Mehmood et al., 2017). The Gibbs free energy change (ΔG) accounts for the available energy for thermal conversion and is found in the range of 170 to 180kJ/mol for all the kinetic models. The change in entropy is both positive and negative (Table 8.4). It varies in the range of -33.64J/K.mol to 65.66J/K.mol. Negative values of ΔS show that the degree of randomness of the products is lower than that of the reactants while in case of positive values it shows that product is in stable condition therefore, the product formation is easy in the previous case. The +ve value of ΔG, ΔH, and ΔS indicates a non-spontaneous reaction has occurred and dependent on the heat introduced to the process during the pyrolysis all the samples

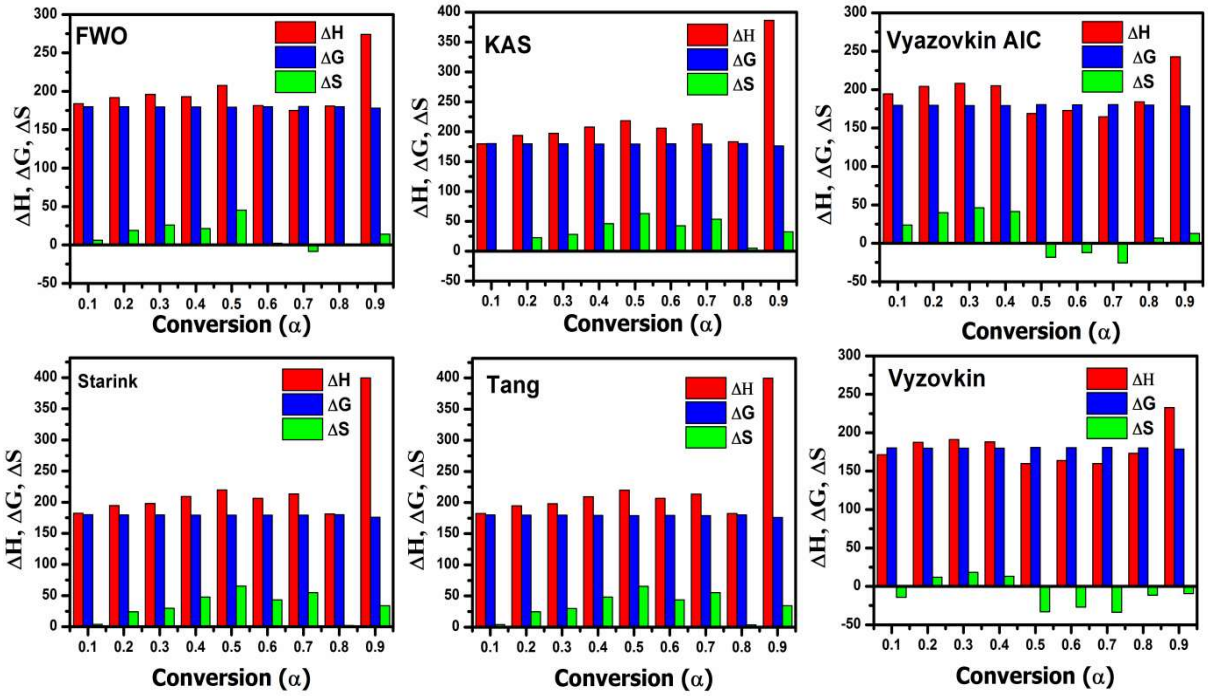


**Fig. 8.5** Variation of thermodynamic parameters with conversion calculated using different models

### 8.10.6. Reaction mechanism

The possible reaction mechanism for the pyrolysis of PS has been predicted using expressions listed in Table 4.2 and developed by Criado et al (1989). The experimental and theoretical z-master curves are compared in Fig. 8.6. It is seen that the experimental curve does not follow any single reaction path throughout the pyrolysis process due its complex nature. For $\alpha < 0.1$, it follows the theoretical curves for $F_1$ (nucleation with one nucleus on the individual particle), $D_1$ (one-dimensional diffusion), $D_2$ (two-dimensional diffusion-Valensi model)) and $D_3$ (three-dimensional diffusion-Jander model). For $\alpha = 0.2$ and 0.5 it closely follows the phase boundary-controlled reaction ($R_2$ contracting area type) and from 0.5 to 0.9 it follows the phase boundary-controlled reaction ($R_2$ -contracting area and, $R_3$ -

contracting volume types). After the release of moisture and lighter volatile matter (at low values of conversion) the degradation of biomass continues through the decomposition of long chain cellulose and hemicellulose molecules forming low molecular weight (or small chain molecules) species that act as the sites for irregular nucleation. The cellulose and hemicellulose contents of peanut shell biomass are mainly amorphous in nature that may permit better exchange of heat to the inside of the particles causing the development of nucleation sites for the advancement of the thermal decomposition (Kumar et al., 2019a).

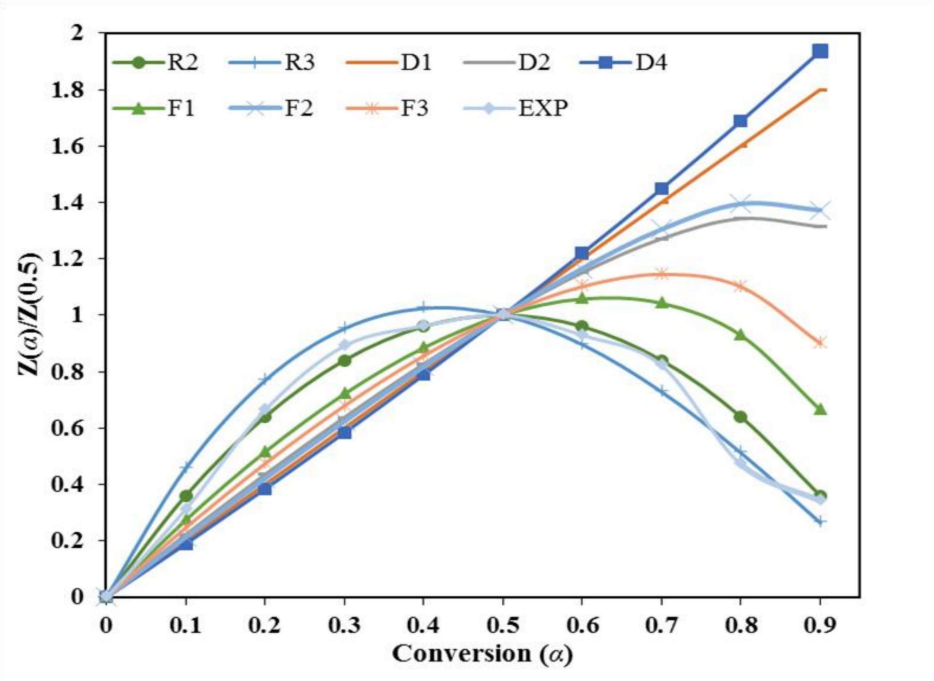


**Fig. 8.6** Comparison of experimental and theoretical reaction mechanism curves

### 8.10.7. The Box-Behenken design

The BBD matrix shown in Table 8.5 includes three independent variables (temperature, heating rate and carrier gas flow rate) and two dependent parameters (bio-oil and bio-char yield). The standard least squares method was utilized with the incorporation of the

independent process parameters that influenced the bio-oil and bio- yields. The analysis was carried out at 3 levels (-1, 0, 1) with total of 17 experimental sets (Table 8.1) to optimize the effect of temperature, heating rate and carrier gas flow rate. The enhancement of the bio-oil and minimization of the bio-char yields were examined as the response of the process. Further, to develop the mathematical relationship between the dependent variable (i. e. the response) and the independent variables (i. e. the process variables) the regression analysis approach has been adopted. Figure 8.7 shows the closeness of the experimental and predicted results for the bio-oil and bio-char yields. The deviation of the experimental results from the predicted ones was judged on the basis of the correlation coefficient (a strong coefficient ($R^2$) and was found to be negligible. The results indicate a strong connection between the prediction and the actual outcome and the model can be used to foresee the yields of the bio-oil and bio-char that could be obtained through the pyrolysis of PS.

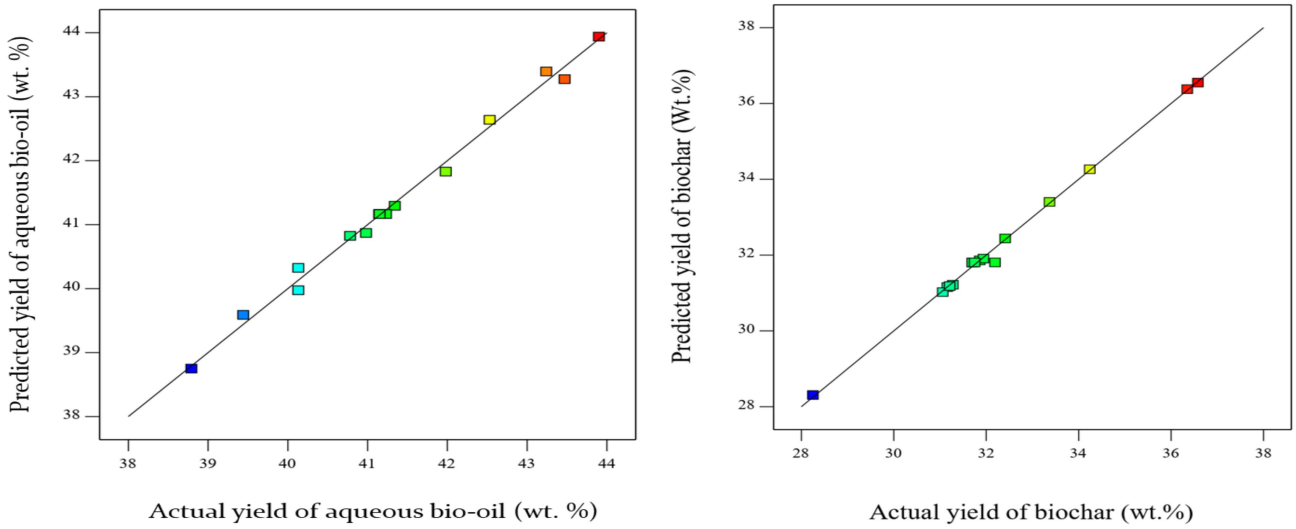


**Fig. 8.7** Comparison of the predicted and experimental values of % aq. bio-oil and bio-char

**Table 8.5:** Box-Behenken design matrix for aq. bio-oil and bio-char production

| Run | A:Temperature (°C) | B:Heating rate (°C/min) | C:Nitrogen flow rate (ml/min) | Bio-oil yield (wt. %) | | Bio-char yield (wt. %) | |
|---|---|---|---|---|---|---|---|
| | | | | Predicted | Experimental | Predicted | Experimental |
| 1 | 525 | 15 | 100 | 41.17 | 41.15 | 31.81 | 31.70 |
| 2 | 650 | 15 | 150 | 43.94 | 43.9 | 31.03 | 31.06 |
| 3 | 525 | 10 | 50 | 40.32 | 40.13 | 34.27 | 34.24 |
| 4 | 650 | 15 | 50 | 41.30 | 41.34 | 31.16 | 31.16 |
| 5 | 650 | 20 | 100 | 43.40 | 43.24 | 28.31 | 28.25 |
| 6 | 525 | 15 | 100 | 41.17 | 41.23 | 31.81 | 31.70 |
| 7 | 525 | 15 | 100 | 41.17 | 41.15 | 31.81 | 31.70 |
| 8 | 650 | 10 | 100 | 41.83 | 41.98 | 31.86 | 31.86 |
| 9 | 525 | 10 | 150 | 42.64 | 42.53 | 32.44 | 32.41 |
| 10 | 400 | 15 | 50 | 38.75 | 38.79 | 33.40 | 33.37 |
| 11 | 400 | 10 | 100 | 39.98 | 40.13 | 31.22 | 31.28 |
| 12 | 525 | 15 | 100 | 41.17 | 41.15 | 31.81 | 32.19 |
| 13 | 525 | 20 | 50 | 40.87 | 40.98 | 31.91 | 31.94 |
| 14 | 525 | 20 | 150 | 43.27 | 43.47 | 31.18 | 31.21 |
| 15 | 400 | 20 | 100 | 39.59 | 39.44 | 36.55 | 36.58 |
| 16 | 400 | 15 | 150 | 40.83 | 40.78 | 36.38 | 36.35 |
| 17 | 525 | 15 | 100 | 41.17 | 41.15 | 31.81 | 31.75 |

### 8.10.8 Pyrolysis experiments

The pyrolysis of (PS) was carried out under optimized conditions (heating rate, temperature and nitrogen flow rate) obtained through the RSM for obtaining the bio-oil and bio-char in the temperature range of 400 to 650$^{o}$C. The lower temperature leads only to the removal of moisture and other lighter organic molecules while at higher temperature breakdown of the long polymeric chain compounds such as hemicellulose and cellulose to smaller hydrocarbon molecules contributing to the bio-oil yield and their further degradation to the non-condensable gaseous products (Kumar et al., 2019c; Charusiri et al., 2017). It is observed that the yield of bio-oil increases with increasing temperature. This may be attributed to the formation of more condensable vapour (David et al., 2018). On the other hand the yield of the bio-char was found to decrease with increasing temperature. The decreasing amount of bio-char with rising temperature is due to the initiation of the secondary decomposition reactions leading to the formation of condensable and non-condensable gases (Charusiri et al., 2017; Gupta et al., 2019). Similar, behaviour was also reported for the pyrolysis of pine wood (Wang et al., 2017), grape bagasse (Demiral et al., 2011), brown salwood (Charusiri et al., 2017) and saw dust (Gupta et al., 2019).

The effects of other parameters such as the flow rate of carrier gas (nitrogen) and the heating rate were also studied. These are also important in view of the bio-oil production. It was found that the bio-oil yield increased with increase in the heating rate due to rapid depolymerisation of the solid biomass material.

### 8.10.9 ANOVA analysis

The analyses of variance (ANOVA) for the bio-oil and bio-char yields have also been carried out and the results are depicted in Tables 8.6 and 8.7, respectively. The model equations generated using the BB design for the bio-oil and bio-char yields are describe by Eq. 8.15 and Eq. 8.16, respectively.

$$Aqueous\ bio-oil\ yield(wt.\%) = 44.23 + 1.51A - 1.74B + 2.78C - 003AB + 0.26AC - 0.12BC - 3.86A^2 - 1.04B^2 - 1.11C^2 \quad (8.15)$$

$$Bio-char\ yield(wt.\%) = 26.97 - 3.50A - 1.06B - 0.81C - 0.13AB - 0.032AC - 0.35BC + 2.71A^2 - 0.22B^2 - 0.20C^2 \quad (8.16)$$

where A, B and C indicate temperature, heating rate and carrier gas (nitrogen) flow rate, respectively.

The F values of 113.29 for the bio-oil and 245.05 for the bio-char suggest that the model is significant. Further the ANOVA quadratic equation also exhibits that the model is critical for the bio-oil and bio-char production with $p < 0.0001$ of the F test values. The p values under 0.0500 show that the model terms are critical, though the p values more than 0.1000 are insignificant. Thus, the model may be considered as sufficient as per the F test. The F-value for "lack of fit" that depicts the appropriateness of the developed quadratic model is an extra essential element for the ANOVA and its higher values as unwanted. The 'lack-of-fit' should not be significant as indicated in Table 8.6 and 8.7for bio-oil and bio-char, respectively for a decent and immaculate model fitting (Gupta et al., 2019). The lack-of-fit

value was found to be 2.23 for aq. bio-oil and 2.12047 for bio-oil and $p > 0.0500$ portrays it is not significant.

The results of ANOVA for the bio-oil and bio-char yields are presented in Table 8.6. It can be noted that the standard deviations (SD) of 0.46 and 0.21 for the pyrolytic products are very small and indicate a very good fit of the optimization model. Mean of ANOVA for the bio-oil and bio-char yields were found to be 41.24 and 29.06%, respectively. The overall standard deviations of the respective experimental data are measured by the co-efficient of variance (CV. %).The CV % for the bio-oil and bio-char yields is 1.38 and 0.87%, respectively. A low CV % (<10%) portrays higher unwavering quality and great reproducibility of the developed model (Kumar et al., 2019c). The correlation coefficient ($R^2$) for the bio-oil and bio-char yields is0.9916 and 0.9956, respectively, which excellent fitting of the model. The adjusted and predicted $R^2$ are the two different parameters that are contemplated in the ANOVA. For the bio-oil and bio-char yields the adjusted $R^2$ values are found to be 0.9848 and 0.9925and the predicted $R^2$ values are 0.9645 and 0.9756, respectively. It is seen that the predicted $R^2$ is in concurrence with the adjusted $R^2$. For adequate precision the noise to signal proportion and its value more than 4 is recommended. The values of adequate precision for bio-oil and bio-char are found to be 35.18and 56.89, respectively which show adequate signal. In this way the above models are effective to work on the design space.

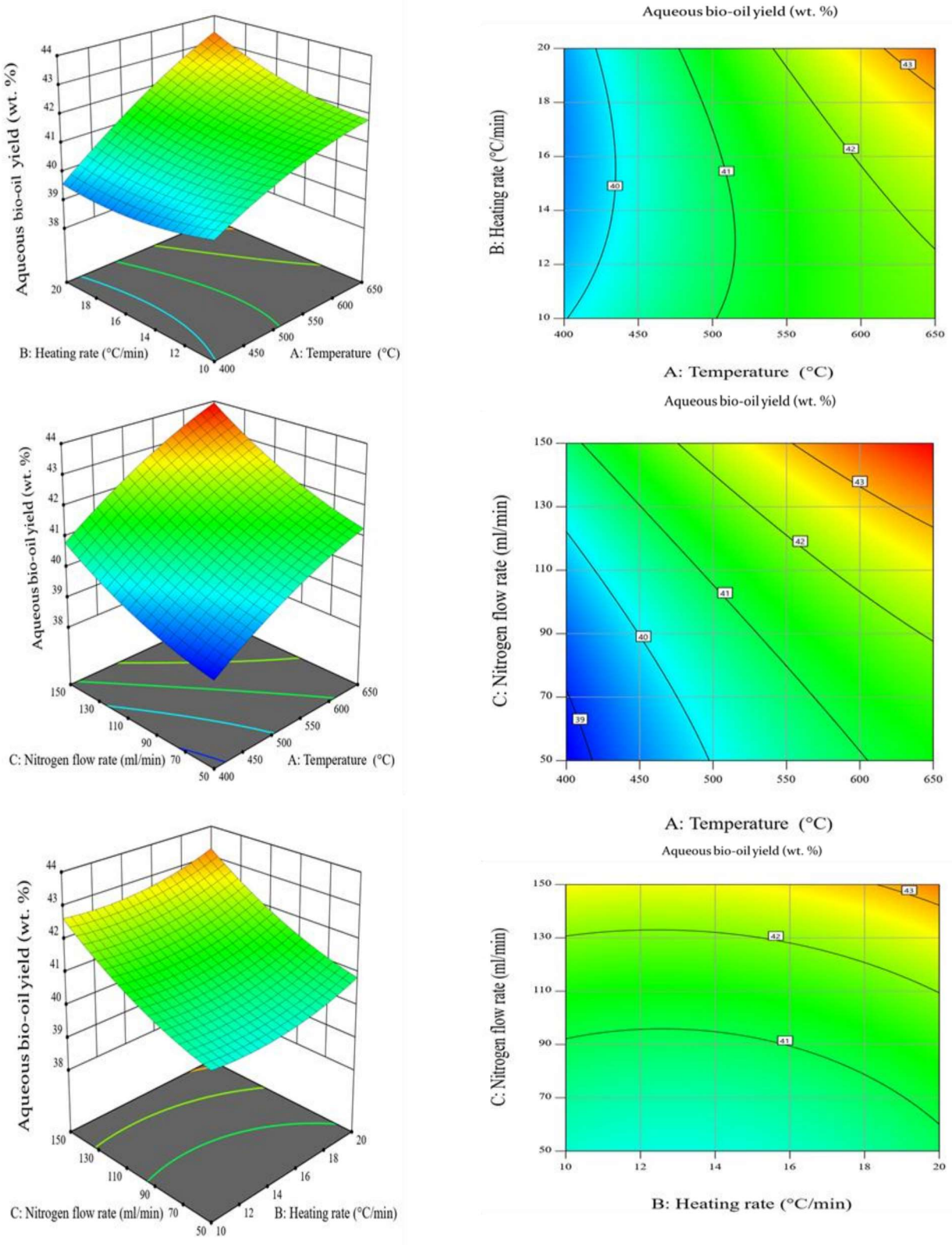


**Fig. 8.8**: 3 Dimensional and contour plots of aqueous bio-oil yields

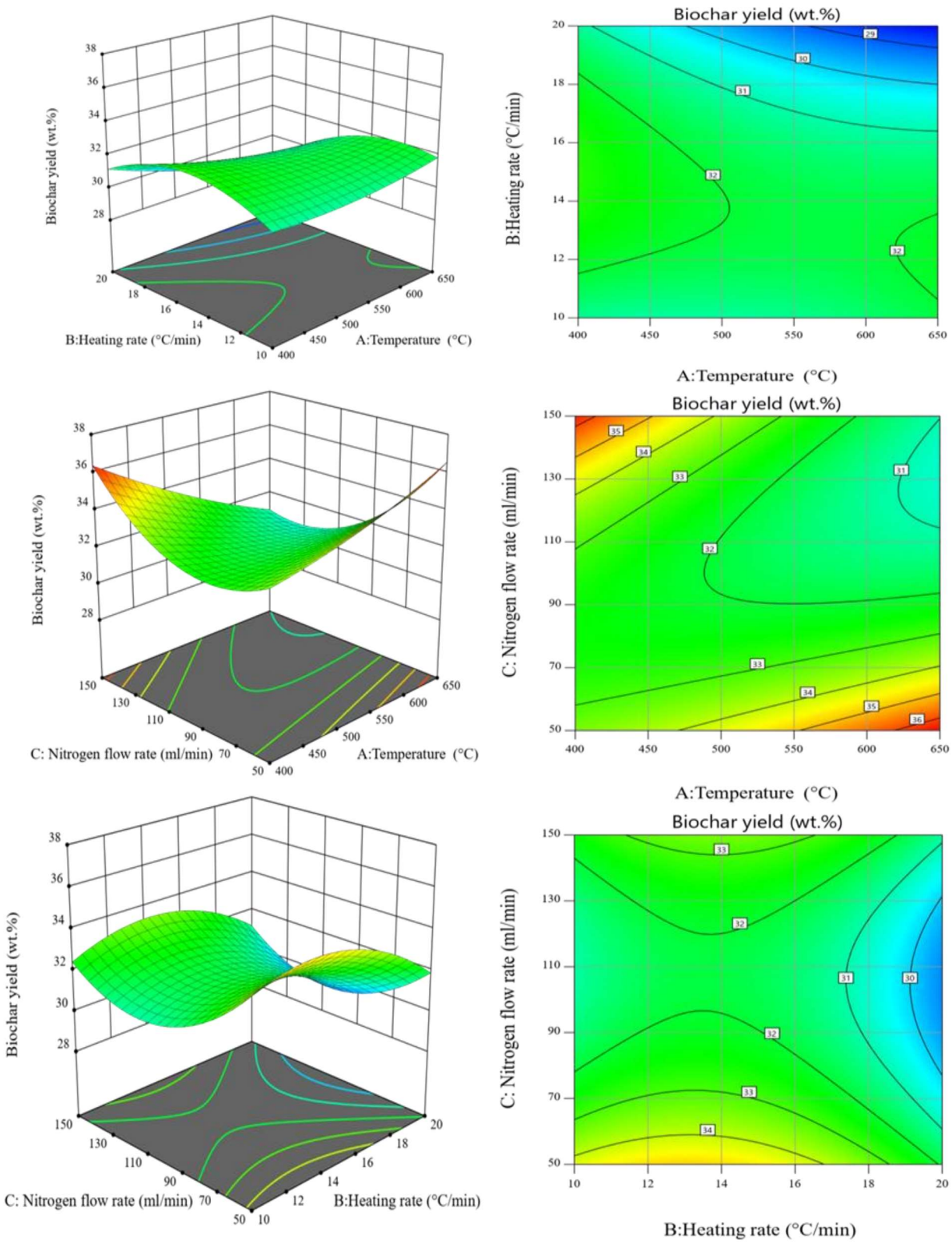


**Fig.8.9**. 3-Dimensional and contour plots of bio-char yields

**Table 8.6:** ANOVA analysis of aqueous bio-oil production

| Source | Sum of Squares | Df | Mean Square | F-value | p-value | |
|---|---|---|---|---|---|---|
| Model | 29.96 | 9 | 3.33 | 113.29 | < 0.0001 | Significant |
| A-Temperature | 16.02 | 1 | 16.02 | 545.17 | < 0.0001 | |
| B-Heating rate | 0.6962 | 1 | 0.6962 | 23.70 | 0.0018 | |
| C-Nitrogen flow rate | 11.14 | 1 | 11.14 | 379.12 | < 0.0001 | |
| AB | 0.9506 | 1 | 0.9506 | 32.35 | 0.0007 | |
| AC | 0.0812 | 1 | 0.0812 | 2.76 | 0.1403 | |
| BC | 0.0020 | 1 | 0.0020 | 0.0689 | 0.8005 | |
| $A^2$ | 0.3109 | 1 | 0.3109 | 10.58 | 0.0140 | |
| $B^2$ | 0.3872 | 1 | 0.3872 | 13.18 | 0.0084 | |
| $C^2$ | 0.4001 | 1 | 0.4001 | 13.62 | 0.0078 | |
| Residual | 0.2057 | 7 | 0.0294 | | | |
| Lack of Fit | 0.2005 | 3 | 0.0668 | 2.23 | 0.0012 | Not-significant |
| Pure Error | 0.0051 | 4 | 0.0013 | | | |
| Cor Total | 30.16 | 16 | | | | |

**Table 8.7**: ANOVA analysis of bio-char production

| Source | Sum of Squares | Df | Mean Square | F-value | p-value | |
|---|---|---|---|---|---|---|
| Model | 62.62 | 9 | 6.96 | 245.05 | < 0.0001 | significant |
| A-Temperature | 2.43 | 1 | 2.43 | 85.62 | < 0.0001 | |
| B-Heating rate | 6.53 | 1 | 6.53 | 230.13 | < 0.0001 | |
| C-Nitrogen flow rate | 3.25 | 1 | 3.25 | 114.51 | < 0.0001 | |
| AB | 3.05 | 1 | 3.05 | 107.24 | < 0.0001 | |
| AC | 18.06 | 1 | 18.06 | 636.15 | < 0.0001 | |
| BC | 0.3025 | 1 | 0.3025 | 10.65 | 0.0138 | |
| $A^2$ | 0.5449 | 1 | 0.5449 | 19.19 | 0.0032 | |
| $B^2$ | 9.86 | 1 | 9.86 | 347.25 | < 0.0001 | |
| $C^2$ | 19.87 | 1 | 19.87 | 699.74 | < 0.0001 | |
| Residual | 0.1988 | 7 | 0.0284 | | | |
| Lack of Fit | 0.0145 | 3 | 0.0048 | 2.1047 | 0.9530 | Not significant |
| Pure Error | 0.1843 | 4 | 0.0461 | | | |
| Cor Total | 62.82 | 16 | | | | |

### 8.10.10 3-D and contour plots

To know the impact of independent variables (temperature, heating rate and nitrogen flow rate) on dependent variables, three-dimensional surface plots and two dimensional contour plots have been developed. These plots are prepared by changing two parameters and keeping the third parameter constant as shown in Fig 8.8 and Fig 8.9 for the bio-oil and bio-char, respectively.

#### 8.10.10.1 Optimization of the temperature and heating rate

The three dimensional surface and two dimensional contour plotsfor temperature and heating rate at constant nitrogen flow rates are shown in Fig. 8.8(a) and 8.9(a) for the bio-oil and bio-char yield, respectively. The 3D-surface plot is used to obtain the three dimensional surface shapes for different values of parameters used and show their effect on the percent yield of bio-oil (Bordoloi et al., 2015). The most direct way to understand the response surface is to look at thecontour plotof the fitted model. In the situation where there are just two or three process factors, the development and understanding of this plot is generally simple. It can be seen from Fig. 8.8(a) and 8.9(a) that, the yield of bio-oil increases as with pyrolysis temperature and heating rate. More volatiles are delivered with increase in temperature due to breaking of the higher organic molecules into the lower molecular weight compounds. The temperature and heating rate contour plot (Fig. 8.8(a) shows outcomes comparable with the 3D-surface plots. It is clearly seen that increasing amount of bio-oil can be obtained at around 525 to 650$^{o}$C using the heating rate of 10–20$^{o}$C/min. The variation of bio-char production with temperature and heating rate keeping the gas flow rate constant is shown in Fig 8.9(a). A diminishing trendy observed in the bio-

char yield with rising temperatures. This is because of more devolatilization of the biomass constituents with increasing temperature (Gupta et al., 2019). The highest bio-oil and lowest bio-char yields are found to be at 650$^{o}$C reaction temperature and 20$^{o}$C/min heating rate.

**8.10.10.2 Optimization of the nitrogen flow rate and temperature**

The 3D and 2D surface plots exhibiting the behaviour of bio-oil and bio-char yields with change in nitrogen gas flow rate and temperature keeping the heating rate constant are depicted in Fig. 8.8(b) and 8.9(b) .It can be seen from Fig. 8.8(b) that as the temperature increases the yield of bio-oil increases. On the other hand with increasing flow rate of the carrier gas the bio-oil yield initially rises but after certain flow rate it decreases. The increase in the bio-oil yield with increasing temperature and career gas flow rate (at low flow) is due the formation of more and more condensable fractions due to increasing thermal degradation and interaction between degradation products of PS. The observed decrease at the higher gas flow rates can be attributed to the less time available for the thermal degradation products to interact with each other to form higher condensable organic molecules. The behaviour of the plot for bio-char production with varying nitrogen flow rate and temperature is depicted in Fig 8.9(b). It is seen that the bio-char yield decreases with increasing nitrogen flow rate and temperature. The higher bio-oil yield and minimum bio-char yield were obtained at 650$^{o}$C and at the nitrogen flow rate of 130ml/min.

#### 8.10.10.3 Optimization of the nitrogen flow and heating rates

Figure 8.8(c) and 8.9(c) depict the 3D and 2D surface response plots prepared by varying the flow rate of nitrogen gas and heating rate and keeping the temperature constant. It is seen that as the flow rate of the carrier gas and heating rate increase the bio-oil yield increases up to a certain limit. With increasing heating and nitrogen gas flow rates, the bio-char yield increases slightly up to a certain value and thereafter it decreases. The maximum bio-oil yield area is found to before the heating rate of 15-20$^{o}$C/min and the nitrogen gas flow rate of 100-150ml/min. The minimum bio-char yield was found to be at the gas flow rate of 110mL/min and heating rate of 15$^{o}$C/min.

#### 8.10.10.4. Validation of the optimum results

For the highest bio-oil and the least bio-char yield, the process variables such as temperature ($^{o}$C), heating rate ($^{o}$C/min) and flow rate of nitrogen (ml/min) were optimised within the selected experimental conditions. The predicted outcome has demonstrated that the temperature of around 650$^{o}$C, heating rate of around 20$^{o}$C/min and nitrogen gas flow rate of around 100mL/min are adequate for the optimum bio-oil production. To experimentally verify these results pyrolysis experiments were carried out at the optimized conditions in triplicate. The experimental and predicted results are presented in Table 8.8. The average values of bio-oil and bio-char yields at the optimum condition were found to be 43.24 and 28.25%, respectively. The deviation between the experimental and model predicted values is of the order of 0.46% and 0.21% for bio-oil and bio-char, respectively. These conditions of gas flow rate, heating rate and temperature thus can be used for maximizing the bio-oil and minimizing the bio-char production.

**Table 8.8**: Summary of ANOVA analysis

| Products | Standard deviation | Means | Co-efficient of variance (%) | $R^2$ | Adjusted $R^2$ | Predicted $R^2$ | Adequate precision |
|---|---|---|---|---|---|---|---|
| Bio-oil | 0.46 | 41.24 | 1.38 | 0.9916 | 0.9848 | 0.9645 | 35.18 |
| Biochar | 0.21 | 29.06 | 0.87 | 0.9956 | 0.9925 | 0.9756 | 56.89 |

### 8.10.11Characterization of products

#### 8.10.11.1 Physicochemical properties of aqueous bio-oil

The liquid condensate (aq. bio-oil) contains both organic as well as aqueous phases. The collected condensed liquid product from bottom of the condensing unit was extracted with dichloromethane ($CH_2Cl_2$) in order to separate the aqueous and organic and phases (Charusiri et al (2017).The organic phase was used for analysis and characterization. Various physicochemical characteristics of the bio-oil (organic phase) produced from pyrolysis of PS at the optimum conditions are summarised in Table 8.9. The bio-oil is acidic in nature (pH = 3.12). The acidity of bio-oil is mainly due to the presence of carboxylic acids, phenolic compounds, and their derivatives (Kumar et al., 2009). The acid number was estimated by titration method using N, N-dimethyl formaldehyde and methanol as the solvent. It was estimated to be 58mgKOH/g. This indicates the corrosive nature of bio-oil. Approximately 5wt% moisture was estimated in the condensed bio-oil obtained from pyrolysis of PS. This value estimated moisture content is more or less similar to that reported by David et al (2018); Charusiri et al (2017) and Mohammed et al (2017) for bio-oil obtained from the pyrolysis of rapeseed de-oil cake, sugar cane leaves and peanut shell, respectively. The density of bio-oil is more than diesel due to the presence of oxygenated heavy organic compounds such as phenols (Ozawa et al.,

1965).The Ramsbottom carbon residue (RCR), the carbon forming property of the oil at high temperatures is 3.59wt. %. The ash content the bio-oil is estimated to be 0.08 wt. % which is in the acceptable range. The higher heating values found to be 24.01MJ/kg, indicating the bio-oil to be a good fuel.

**Table 8.9**: Physicochemical properties of bio-oil sample

| Properties | Aq. Bio-oil |
|---|---|
| Appearance | Dark brown |
| pH | 3.12 |
| Acidity($mg_{KOH}/g$) | 58 |
| Moisture content (wt %) | ~5 |
| Density($kg/m^3$) | 1015 |
| Kinetic viscosity ($mm^2/s$) | 46 |
| Ramsbottom carbon residue (wt. %) | 3.59 |
| HHV (MJ/kg) | 26.49 |
| Ash Content (wt. %) | 0.08 |

### 8.10.11.2 FTIR analysis of aqueous bio-oil

The FTIR spectrum of bio-oil is showing in Fig. 8.2. The broad peak around $3500cm^{-1}$ confirms the presence O-H groups of phenol, alcohol, polymeric OH and water molecules (Vyazovkin et al., 2006; Kim et al., 2018). The strong peak at around $1700cm^{-1}$ confirms the C = O stretching vibration which indicates the presence of ketone, quinines, aldehyde and carboxylic acid compounds (Kumar et al., 2019b). The low intensity peak at $1600cm^{-1}$ is attributed to the C = C stretching and may be due to the presence of alkene bond (Kumar et al., 2019b). The medium intensity peak at $1400cm^{-1}$ is because of the C-H bending in alkanes and substituted aromatic compounds. The peaks at around 1200 and $1000cm^{-1}$ are

due to the C-O stretching and O-H deformation and confirm the presence of alcohols, phenols, ethers and esters. The small peaks observed below 1000cm$^{-1}$indicate the presence of mono, polycyclic, and substituted, aromatic compounds.

It can be inferred that the bio-oil contains oxygenated organic compounds such as acids, phenols, sugars, hydroxyl-aldehydes, hydroxyl-ketones and alcohols. This leads to heterogeneity in the bio-oil which in turn affects the energy density, storage stability, and its miscibility with hydrocarbon fuels (Chatterjee et al., 2018).

**8.10.11.3 GCMS analysis of bio-oil**

Various organic compounds present in the bio-oil and identified through GCMS analysis are in Table 8.10together with their retention time, chemical name, molecular formula and % area covered. It is observed that the phenolic compounds and their derivatives are the primary constituents of the bio-oil. The major phenolic and other compounds include phenol 2-methoxy-, 3-methylcyclopentane-1,2-dione, creosol,phenol 4-ethyl-2-methoxy-, 2-furanmethanol, 2-cyclopenten-1-one, 2-methyl, N-(n-Butoxymethyl)acrylamide, 2, cyclopenten-1-one, 3-methyl-, 2-methyl-3-hexanone, 2-cyclopenten-1-one, 3-ethyl-2-hydroxy-, 1,4:3,6-dianhydro-.alpha.-d-glucopyranose, phenol, 2,6-dimethoxy-, 5-methyl-1,3-benzenediol, phenol, 2-methoxy-4-(1-propenyl)-, and 2-propanone, 1-(4-hydroxy-3-methoxyphenyl) and are due to the decomposition of lignin. Simultaneous degradation of lignin and cellulose gives rise to production of aldehydes, ketones, and ester related compounds and also some oxygenated organic compounds. Acidic compounds and their derivative such as acetic acid butanoic (or butyric) acid, etc. are formed mainly due to the decomposition of hemicellulose. The degradation of cellulose also produces laevoglucose

compounds such as 1, 6- anhydro- beta. – D-glucopyranose together with furan and their derivatives which are detected in the bio-oil. Aliphatic organics, aldehydes, ketones, esters, alcohols and some of the carboxylic acids presents in the bio-oil are derived from the cellulose and hemicellulose (Biswas et al., 2017). The nitrogenous compounds like pyridine, 2-ethyl-, N-(n-butoxymethyl) acrylamide, pyridine2, 5-dimethyl- etc. Present in the bio-oil may be attributed to the protein based compounds of raw PS. The ring and straight chain hydrocarbons like2,3-hexadiene, 2-methyl- cyclopropene, 1-butyl-2-ethyl-, hexane, 2,2,4-trimethyl-naphthalene, 1-methyl- etc. are mainly due to the decomposition of acidic compounds present in the PS.

**Table 8.10**: GCMS analysis of bio-oil

| R. Time | Name | Molecular formula | Area% |
|---|---|---|---|
| 6.632 | 2-Furanmethanol | $C_5H_6O_2$ | 3.23 |
| 7.253 | 2-Cyclopenten-1-one, 2-methyl | $C_6H_8O$ | 1.86 |
| 6.358 | 2,3-Hexadiene, 2-methyl- | $C_7H_{12}$ | 0.30 |
| 7.385 | Ethanone, 1-(2-furanyl)- | $C_6H_6O_2$ | 0.77 |
| 7.628 | Pyridine, 2-Ethyl- | $C_7H_9N$ | 0.21 |
| 7.864 | N-(n-Butoxymethyl) acrylamide | $C_8H_{15}NO_2$ | 1.70 |
| 7.938 | Acetic acid, 2-(dimethylamino) ethyl ester | $C_6H_{13}NO_2$ | 0.16 |
| 8.062 | 2-Cyclopenten-1-one, 2,3-dimethyl- | $C_7H_{10}O$ | 0.18 |
| 8.275 | Cyclopropene, 1-butyl-2-ethyl- | $C_9H_{16}$ | 0.13 |
| 8.356 | Pyridne, 2,5-Dimethyl- | $C_7H_9N$ | 0.30 |
| 9.014 | 2-Butanone, 1-chloro- | $C_4H_7ClO$ | 0.18 |
| 9.118 | 2-Cyclopenten-1-one, 3-methyl- | $C_6H_8O$ | 1.43 |
| 9.411 | 2(5H)-Furanone, 3-Methyl- | $C_5H_6O_2$ | 0.24 |
| 9.622 | 2-Furanmethanol, Acetate | $C_7H_8O_3$ | 0.09 |
| 9.728 | 2-Cyclopenten-1-one, 2,3-Dimethyl- | $C_7H_{10}O$ | 0.44 |
| 10.026 | Phenol | $C_6H_6O$ | 1.14 |

| | | | |
|---|---|---|---|
| 10.166 | 2-Methyl-3-Hexanone | $C_7H_{14}O$ | 1.02 |
| 10.333 | 2,4-Dimethyl-2-oxazoline-4-methanol | $C_6H_{11}NO_2$ | 0.34 |
| 10.516 | 2-Amino-4-methylpyrrole-3-carbonitrile | $C_6H_7N_3$ | 0.15 |
| 11.038 | 3-Methylcyclopentane-1,2-dione | $C_6H_8O_2$ | 6.52 |
| 11.361 | 3-Ethyl-3-pentyl methylphosphonofluoridate | $C_8H_{18}FO_2P$ | 0.35 |
| 11.600 | 4-Isopropylcyclohexylamine | $C_9H_{19}N$ | 0.35 |
| 11.737 | 3,5-Dimethyl Cyclopentenolone | $C_7H_{10}O_2$ | 0.35 |
| 11.970 | Phenol, 2-Methyl- | $C_7H_8O$ | 0.53 |
| 12.216 | 3-Octen-2-ol, (Z)- | $C_8H_{16}O$ | 0.17 |
| 12.308 | 3,4-Dimethyl Cyclopentenolone | $C_7H_{10}O_2$ | 0.17 |
| 12.505 | Phenol, 2-methoxy- | $C_7H_8O_2$ | 11.45 |
| 12.605 | Phenol, 2-methoxy- | $C_7H_8O_2$ | 8.26 |
| 13.042 | Hexane, 2,2,4-trimethyl- | $C_9H_{20}$ | 0.52 |
| 13.148 | 1-Penten-3-ol | $C_5H_{10}O$ | 1.03 |
| 13.430 | 4H-Pyran-4-one, 3-Hydroxy-2-Methyl- | $C_6H_6O_3$ | 0.75 |
| 13.588 | 2-Cyclopenten-1-one, 3-ethyl-2-hydroxy- | $C_7H_{10}O_2$ | 1.82 |
| 14.357 | 1,6-Cyclodecadiene | $C_{10}H_{14}O_2$ | 0.50 |
| 14.710 | Phenol, 3,5-Dimethyl- | $C_8H_{10}O$ | 0.64 |
| 14.913 | N-(2,3,5-Triazolyl)- Acetamide | $C_4H_6N_4O$ | 0.17 |
| 15.071 | 2-Methoxy-6-methylphenol | $C_8H_{10}O_2$ | 0.30 |
| 15.233 | Phenol, 4-ethyl- | $C_8H_{10}O$ | 0.18 |
| 15.350 | Levomenthol | $C_{10}H_{20}O$ | 0.14 |
| 15.552 | Creosol | $C_8H_{10}O_2$ | 6.07 |
| 16.055 | 2-Cyclopenten-1-one, 2-Hydroxy-3-Propyl- | $C_8H_{12}O_2$ | 0.36 |
| 16.338 | Dianhydromannitol | $C_6H_{10}O_4$ | 0.35 |
| 16.526 | 1,4:3,6-Dianhydro-.alpha.-d-glucopyranose | $C_6H_8O_4$ | 1.24 |
| 16.788 | 3,4-Dimethoxytoluene | $C_9H_{12}O_2$ | 0.21 |
| 16.971 | Benz aldehyde, 4-(1-methylethyl)- | $C_{10}H_{12}O$ | 0.69 |
| 17.388 | 2-Octen-1-ol, 3,7-dimethyl-, isobutyrate, (Z)- | $C_{14}H_{26}O_2$ | 0.32 |
| 17.710 | n-Propyl benzoate | $C_{10}H_{12}O_2$ | 0.23 |
| 17.903 | Phenol, 4-ethyl-2-methoxy- | $C_9H_{12}O_2$ | 5.92 |

| | | | |
|---|---|---|---|
| 18.448 | Naphthalene, 1-Methyl- | $C_{11}H_{10}$ | 0.32 |
| 18.950 | 2-Methoxy-4-vinylphenol | $C_9H_{10}O_2$ | 0.43 |
| 19.691 | 2(3H)-Furan one, 5-Butyldihydro- | $C_8H_{14}O_2$ | 0.18 |
| 19.934 | Phenol, 2,6-dimethoxy- | $C_8H_{10}O_3$ | 1.93 |
| 20.275 | Phenol, 2-methoxy-4-propyl- | $C_{10}H_{14}O_2$ | 0.51 |
| 20.526 | 1-Pentyn-3-ol, 3,4-dimethyl- | $C_7H_{12}O$ | 0.16 |
| 20.690 | 1,2-Dioxolan-3-one, 5,5-diethyl-4-methylene- | $C_8H_{12}O_3$ | 0.41 |
| 21.010 | 2-Carbobutoxypyrrole | $C_9H_{13}NO_2$ | 0.31 |
| 21.126 | Hexadecane | $C_{16}H_{34}$ | 0.22 |
| 21.381 | Phenol, 2-methoxy-5-(1-propenyl)-, (E)- | $C_{10}H_{12}O_2$ | 0.61 |
| 21.801 | 5-Methyl-1,3-Benzenediol | $C_7H_8O_2$ | 1.46 |
| 22.192 | 1-Hexanol, 2-Ethyl-, Acetate | $C_{10}H_{20}O_2$ | 0.26 |
| 22.358 | 3,5-Dimethoxy-4-hydroxytoluene | $C_9H_{12}O_3$ | 0.68 |
| 22.525 | Phenol, 2-methoxy-4-(1-propenyl)- | $C_{10}H_{12}O_2$ | 1.56 |
| 23.497 | Ethanone, 1-(4-Hydroxy-3-Methoxyphenyl)- | $C_9H_{10}O_3$ | 0.43 |
| 23.944 | 3-Methoxy-5-propylphenol | $C_{10}H_{14}O_2$ | 0.57 |
| 24.249 | Benzene, 1,2,3-Trimethoxy-5-Methyl- | $C_{10}H_{14}O_3$ | 0.54 |
| 24.460 | 2-Propanone, 1-(4-hydroxy-3-methoxyphenyl)- | $C_{10}H_{12}O_3$ | 1.46 |
| 24.832 | Benzene, 4-butyl-1,2-dimethoxy- | $C_{12}H_{18}O_2$ | 0.15 |
| 25.715 | 3,4-Dimethoxyphenethyl alcohol | $C_{10}H_{14}O_3$ | 0.17 |
| 26.057 | Octadecanoic, 1-chloro- | $C_{18}H_{37}Cl$ | 0.31 |
| 27.345 | Benzene propanol, 4-hydroxy-3-methoxy- | $C_{10}H_{14}O_3$ | 0.41 |
| 28.315 | 2-Undecene, 4,5-dimethyl- | $C_{13}H_{26}$ | 0.12 |
| 29.606 | Ethyl 2,4-dihydroxy-6-methylbenzoate | $C_{10}H_{12}O_4$ | 0.63 |

#### 8.10.11.4 $^{1}$HNMR analysis of bio-oil

The $^{H}$NMR spectrum gives quantitative details the functional group and is used to support the results of FTIR spectra (Mullen et al., 2009). The $^{1}$HNMR spectrum indicated principally two regions, in particular aliphatic and aromatic and hydrogen resonances. The

aliphatic hydrogen resonances happen in the 0.5-6.5 ppm range while the aromatic hydrogen resonances happen in the 6.5-9.0 ppm range. The unfiled area of $^{H}$NMR spectra (0.5 to 1.5 ppm) demonstrates the protons of aliphatic and allylic group atoms. The range of 1.8 to 2.8 ppm relates to the proton of the allylic group atoms present in carbonyls (ketones, esters, aldehydes, acids, and amides) and alkenes or aromatics. The spectra of the 2.8 to 4.5 ppm range correspond to the protons present in ethers and esters correspond to oxygen single bonds and $CH_2$group connected to the two fragrant rings. Tops in the locale of 6.5 to 8.5 ppm relate to the proton of aldehyde gathering (Vyazovkin et al., 2006).

### 8.10.12 Bio-char characterization

#### 8.10.12.1 Physicochemical characteristics

The proximate and elemental analyses results of bio-char are listed in Table 8.11. It is interesting to note that the moisture (1.12%) and volatile matter (10.45%) contents of bio-char are much lower than raw PS sample due to the removal of moisture and volatile matter during pyrolysis. On the other hand the fixed carbon (78.59%) and ash (10.96%) contents are higher compared to those for the raw PS sample. The ash content is comparable to that for coal (Anupam et al., 2016). The lower values of H/C and O/C molar ratios indicate a higher level of carbonization and higher stability of the bio-char, thus indicating a low smoke release and high energy recovery (Chatterjee et al., 2018). The estimated higher heating value (HHV) is 26.96kJ/mol is comparable to HHV for the sawdust bio-char and nearly similar to the values reported by other workers for peanut shell (Table 8.11).The EDX results indicated the presence of Na, Mg, Ca, K, etc., the micro-nutrients required for

the plant growth indicating the suitability of bio-char as a soil amendment (Demirbas et al., 2004).

**Table 8.11**: Physicochemical properties of bio-char

| Analysis | Bio-char |
|---|---|
| **Proximate analysis (wt. %)** | |
| Moisture content | 1.12 |
| Volatile matter | 10.45 |
| Ash content | 10.96 |
| Fixed carbon | 78.59 |
| VM/FC | 0.13 |
| **Ultimate analysis (wt. %)** | |
| C | 81.65 |
| H | 3.14 |
| N | 1.67 |
| S | - |
| O | 13.54 |
| H/C | 0.15 |
| O/C | 0.12 |
| HHV(MJ/kg) | 26.96 |
| **EDX mineral analysis (wt. %)** | |
| Sodium | 4.01 |
| Magnesium | 6.29 |
| Aluminium | 48.56 |
| Silica | 10.16 |
| Potassium | 11.26 |
| Calcium | 9.26 |
| Manganese | 5.63 |
| **BET surface area ($m^2/g$)** | 249.26 |

### 8.10.12.2 FTIR analysis of bio-char

The FTIR spectrum of bio-char is shown in Fig. 8.2. It is seen that the broad peak observed in the raw PS at 3500$cm^{-1}$ has changed to a small sharp intense peak indicating the –OH groups of phenols, alcohols or carboxylic acids and water. The peak at 1500$cm^{-1}$ is due to

the presence of C=C bond of aromatic compounds. Absorption peak at around 1000cm$^{-1}$ is due to the vibration of C-C bonds of ether and ester. Almost all peaks between 1500 and 800cm$^{-1}$ have diminished due to the pyrolysis and removal of organic compounds.

### 8.10.12.3 SEM analysis

The SEM images of bio-char produced at the optimum conditions along with that of the PS powder are shown in Fig. 8.10. It is seen that there are very few pores in the PS biomass sample but the product bio-char is highly porous indicating its suitability as adsorbent and support for catalysts. When used as a soil conditioner it is likely to contribute more to the enhancement of soil quality and act as additional sites for nutrient exchange.

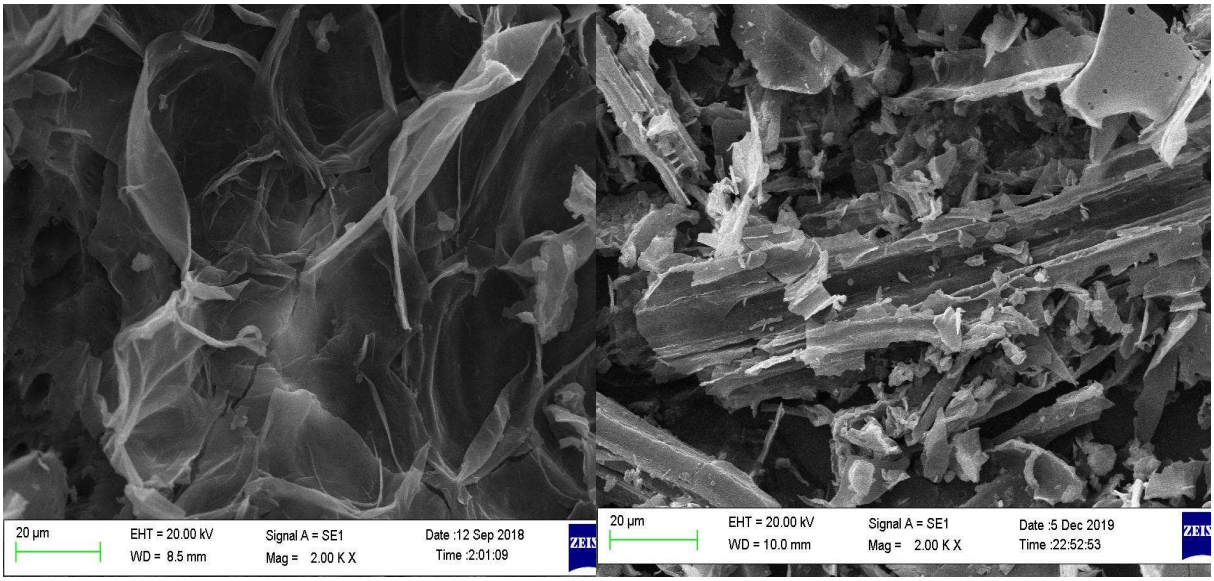


**Fig. 8.10** SEM analysis image of (a) raw peanut shell and (b) biochar sample

## 8.11 Conclusion

The thermo-chemical characteristics and pyrolytic behaviour of peanut shell indicate it to be good feedstock for energy and chemicals. The kinetic analysis of TGA/DTG-temperature data using six iso-conversional models indicate that the lowest average

activation energy (186 kJ/mol) is obtained by the Vyazovkin model and maximum (226.97 kJ/mol) by the KAS model. The enthalpy change is found to be very close to the activation energy for all six models which indicating the feasibility of the pyrolysis for energy generation. The optimization of pyrolysis process using Box-Behenken design resulted in a second order model equation and the optimum temperature of 650$^{o}$C, nitrogen flow rate of 100ml/min and heating rate of 20$^{o}$C/min for obtaining maximum bio-oil and bio-char yields. There is an excellent agreement between experimental and predicted yields. The FTIR, GCMS and $^{H}$NMR techniques have indicated that2-furanmethanol, phenol, 2-methoxy-Creosol, phenol, 4-ethyl-2-methoxy- etc. is the major components of the bio-oil. The product bio-char is highly porous and has high carbon content and heating value indicating its use as soil conditioner, biocatalysts and adsorbent in waste water treatment.